

Optical Engineering

SPIDigitalLibrary.org/oe

Multisegmented, multilayer-coated mirrors for the Solar Ultraviolet Imager

Dennis Martínez-Galarce
Regina Soufli
David L. Windt
Marilyn Bruner
Eric Gullikson
Shayna Khatri
Eberhard Spiller
Jeff C. Robinson
Sherry Baker
Evan Prast

Multisegmented, multilayer-coated mirrors for the Solar Ultraviolet Imager

Dennis Martínez-Galarce

Galapagos Science & Engineering Group
355 1st Street, Suite #407
San Francisco, California 94105
E-mail: dsmartinezg@yahoo.com

Regina Soufli

Lawrence Livermore National Laboratory
7000 East Avenue
Livermore, California 94550

David L. Windt

Reflective X-ray Optics
1361 Amsterdam Avenue
Suite 3B, New York, New York 10027

Marilyn Bruner

Bermar Science & Technology
44 Roosevelt Circle
Palo Alto, California 94306

Eric Gullikson

Lawrence Berkeley National Laboratory
1 Cyclotron Road
Berkeley, California 94720

Shayna Khatri

L-3 Communications IOS-Tinsley
4040 Lakeside Drive
Richmond, California 94806

Eberhard Spiller

Jeff C. Robinson
Sherry Baker

Lawrence Livermore National Laboratory
7000 East Avenue
Livermore, California 94550

Evan Prast

Research Electro-Optics
5505 Airport Boulevard
Boulder, Colorado 80301

Abstract. The Solar Ultraviolet Imager (SUVI) is one of the several instruments that will fly on board the next generation of Geostationary Operational Environmental Satellites R-U platforms, as part of the National Oceanic and Atmospheric Administration's space weather monitoring fleet. SUVI is a generalized Cassegrain telescope that employs multilayer-coated optics that operate in six extreme ultraviolet (EUV) narrow bandpasses centered at 93.9, 131.2, 171.1, 195.1, 284.2 and 303.8 Å. The innovation of the design is that SUVI is the first EUV solar telescope that has six different wavelength channels accommodated on each mirror. And despite having six segmented multilayer-coatings, shadowing (due to the mask) is minimized allowing SUVI to exceed its effective area specifications. Once operational, SUVI will record full-disk, spectroheliograms every few minutes, where this data will be used to better understand the effects of solar produced EUV radiation on Earth and the near-Earth environment. The material presented discusses general aspects of the SUVI optical design, mirror fabrication, super polishing, and metrology carried out to verify optical surface quality and in-band, EUV reflectivity performance of the multilayer coatings. The power spectral density and EUV measurements are shown to exceed performance requirements and are critical for the overall calibration and monitoring of SUVI's throughput and imaging performance, once operational. © 2013 Society of Photo-Optical Instrumentation Engineers (SPIE) [DOI: [10.1117/1.OE.52.9.095102](https://doi.org/10.1117/1.OE.52.9.095102)]

Subject terms: Solar Ultraviolet Imager; extreme ultraviolet solar physics; extreme ultraviolet optics; multilayer-coated optics; power spectral density of extreme ultraviolet optics; extreme ultraviolet scattering; surface microroughness; extreme ultraviolet reflectivity.

Paper 130268P received Feb. 19, 2013; revised manuscript received Aug. 2, 2013; accepted for publication Aug. 9, 2013; published online Sep. 6, 2013.

1 Introduction

Understanding the solar-terrestrial environment and its impact on Earth's global weather and climate is an important problem of modern scientific investigation. Relative influences of "climate forcing," i.e., the various physical mechanisms responsible for driving the Earth's climate, are known to drive Earth's climate: greenhouse gases (anthropogenic), volcanic aerosols, cloud cover, atmospheric composition, water vapor, internal oscillations (El Niño-Southern Oscillation/ENSO,

the North Atlantic Oscillation/NAO and the Quasi-Biennial Oscillation/QBO), and total solar irradiance (TSI in W/m^2),¹ where TSI is the total solar radiative output.

In particular, and related to TSI, are large energetic solar events, such as flares and coronal mass ejections (CMEs) that comprise large energy releases composed of photons and particle masses that are also known to adversely affect Earth and the near-Earth environment, and human-engineered assets (e.g., satellites, aircraft, radio communication systems and ground electrical power grids). TSI is only one component of the total solar energy output, but it is a strong contributor to the physical processes involved in

understanding the nature of space weather and its impact on Earth's weather and climate. As such, TSI is a strong contributor to Earth's temperature, where incoming solar radiation (i.e., with peak flux $\sim 5000 \text{ \AA}$) heats the Earth, whereas outgoing radiation from Earth (with peak flux $\sim 10 \text{ \mu m}$) cools it. The difference in energy yields the amount of heating (or cooling) that determines Earth's average surface temperature which also drives global climate.²

An important component of TSI is extreme ultraviolet (EUV) radiation. EUV radiation that reaches Earth's atmosphere is known to be the catalyst that mostly drives the thermodynamics and chemistry of its upper atmosphere, as well as the thermosphere and ionosphere which are directly coupled to EUV radiation and the electric fields and thermal structure created in these zones which can produce winds of up to 100 km/hr affecting circulation in the lower atmosphere and disrupt global radio communication. EUV light is also a catalyst for chemical cycles in the upper atmosphere including water, ozone, and nitrogen cycles in the Mesosphere (~ 50 to 100 km height).^{3,4} Depletion of the ozone layer by photochemistry is also driven by modulation in EUV radiation, causing "leakage" of higher wavelength UV radiation ($>2000 \text{ \AA}$) to Earth's surface.

It is known that EUV radiation originates in the hot solar chromosphere, transition region, and corona and is produced by very hot, dynamic, ionized plasma that lie in temperature ranges of about, $T \sim 10^4$ to 10^5 K , 10^5 to 10^6 K and $T > 10^6 \text{ K}$, respectively.^{5,6} Understanding the physical mechanisms that produce EUV radiation and how it varies on short (seconds to days) and long (weeks to decades) time-scales is critical to understanding its effect on Earth and the near-Earth environment. As such, the National Oceanic and Atmospheric Administration (NOAA) commissioned a fleet of satellites called the Geostationary Operational Environmental Satellites (GOES) which have on board various instruments to monitor the Sun, Earth, and the near-Earth environments. One of the instruments on board the GOES satellite that will fly on the upcoming GOES "R" + spacecrafts is the Solar UltraViolet Imager (SUVI). SUVI, specially designed to monitor and measure solar EUV radiation in six narrow bandpasses, is the first solar telescope to use a novel, six-segmented, multilayer-coating design that will provide invaluable observations to understand EUV production and its variability and how it affects Earth, space weather, and climate.

2 SUVI Design

The SUVI telescope is a generalized Cassegrain that employs six narrow band EUV channels to image the Sun's radiation produced within its atmosphere. The SUVI optical system consists of multilayer-coated optics (mirrors), thin-film metallic filters and a back-illuminated CCD detector at its focus to record EUV images of the solar disk and its atmosphere (spectroheliograms). Using an aperture selector, SUVI operates at any one of the six EUV passbands via a combination of the thin-film filters and the multilayer-coated optics. SUVI's novelty lies in that each optic of the telescope has six distinct multilayer coatings (deposited as six pie segments), that are fine tuned to reflect at a well-defined EUV wavelength that will be used to "probe" a particular temperature region of the observed solar atmosphere. The six multilayer coatings are designed to reflect at 93.9, 131.2, 171.1, 195.1, 284.2 and 303.8 \AA . Over the course of its mission, SUVI will image, record, and telemeter spectroheliograms taken in these EUV narrow passbands to image the sun's upper atmosphere that consists of the chromosphere, the transition region, and the corona. The use of instruments composed of multilayer-coated optics to observe the Sun's hot and dynamic atmosphere has been a long established experimental technique in solar physics.⁷⁻¹³ SUVI's mission will be to observe and record large energetic solar events, such as flares, CMEs and the solar wind, events that are known to affect Earth and its near-space environment as well as to monitor the sun's long-term EUV production.

The generalized Cassegrain system consists of a concave hyperbolic primary mirror paired with a convex hyperbolic secondary mirror, as shown schematically in Fig. 1. The generalized Cassegrain prescription can be developed from either a classical Cassegrain (parabola/hyperbola) or from a Ritchey-Chrétien (hyperbola/hyperbola) by optimizing the performance over the required field of view with the aid of geometric ray-tracing software. Both techniques were employed for the SUVI design and gave comparable results. The optical description of this hyperboloid-hyperboloid generalized Cassegrain design is given in Table 1.

Table 2 shows the main solar observations intended for SUVI and Fig. 2 is a representative sample of spectroheliograms recorded by the atmospheric imaging assembly (AIA)¹³ and extreme-ultraviolet imaging telescope (EIT)¹¹ in the same passbands as SUVI. SUVI will record similar observations and although SUVI shares some of the same

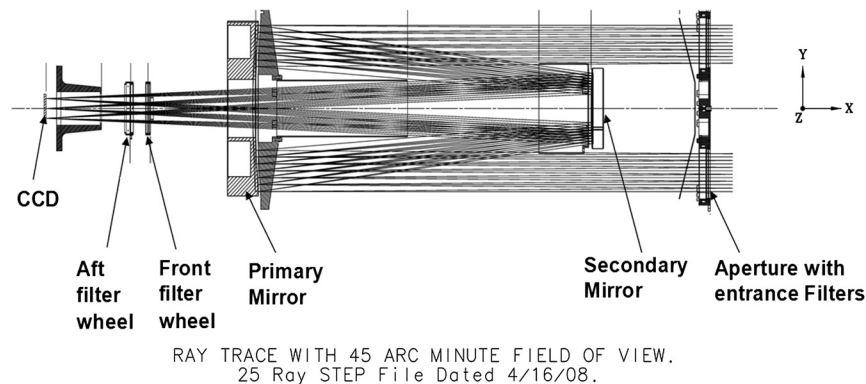


Fig. 1 Ray trace of the Solar Ultraviolet Imager (SUVI) optical system with a hyperbolic primary and secondary mirrors.

Table 1 Solar Ultraviolet Imager (SUVI) optical design.

Quantity	Value
Telescope type	Generalized Cassegrain
Primary mirror diameter	20 cm
Effective focal length	173.04 cm
Number of EUV bandpasses	Six: 93.9, 131.2, 171.1, 195.1, 284.2 and 303.8 Å
CCD pixel size	21 × 21 (μm) ²
Angular pixel size	2.5 × 2.5 (arc sec) ²
Minimum field of view (FOV) required	44 × 44 (arc min) ²
Total CCD array size	1280 × 1280 pixels
FOV with selected array	53.3 × 53.3 (arc min) ²

EUV passbands with the latter instruments, it differs in many ways (which we will not discuss herein but see Refs. 11 and 13 for more discussion on EIT and AIA, respectively), but the primary differences are that the mission and instrument designs of each telescope set them apart. EIT has been operational since 1995 and has been slowly degrading in performance and may soon come to the end of its useful mission. AIA, composed of four telescopes operating at nine EUV/FUV and one visible narrow bandpasses, has higher imaging resolution (~ 1.2 arc sec) and temporal resolution (~ 12 sec cadence) than EIT and SUVI, and has operated since 2010, but has a projected mission lifetime of only 5 years.^{13,14} SUVI, comparable in performance to EIT (but imaging in six EUV channels versus EIT's four), will be on board the GOES-R satellite which is currently scheduled for launch in 2014. The spacecraft will be placed into geosynchronous orbit and then wait to be commissioned to operability when needed. This could occur anytime up to 5 years, postlaunch.

Table 2 Six extreme ultraviolet (EUV) wavelength bands are required to observe the range of solar phenomena important for space weather forecasting. $\text{Log}(T_e)$ refers to the electronic temperature of the observed solar plasma. CME stands for coronal mass ejection.

Wavelength $\text{Log}(T_e)$	93.9 Å 6.8	131.2 Å 5.2, 7.0, 7.2	171.1 Å 5.8	195.1 Å 6.1, 7.3	284.2 Å 6.3	303.8 Å 4.7
Filaments						
Coronal Holes						
Active Region Complexity						
CMEs (e.g. dimming)						
Flare Location and Morphology						
Quiet Regions						

Further, SUVI's operational mission is designed to be over a longer period, spanning a minimum of 10 years.

As SUVI is designed to operate at EUV wavelengths, special attention was given to the fabrication of its optical components and in particular, the mirrors. A figure of merit that is typically used for measuring the quality of a mirror's polished surface is the figure error which measures the RMS surface deviation from the ideal surface prescription at long spatial scales (roughly, on order of the diameter of the optic down to approximately visible wavelength scales). Operation at EUV wavelengths, however, require that one further consider the surface deviations that occur on order of spatial scales ranging from ~ 1 mm down to Angströms. This deviation at these spatial scales is referred to as the RMS microroughness, which we will discuss in detail in Sec. 3. Microroughness affects both instrument throughput and imaging performance, but herein we discuss only the individual mirror measurements and not the system effect on the instrument's imaging and throughput performance. For further discussion regarding SUVI imaging performance, see Refs. 15–17. For discussion regarding effects of mirror roughness and photon scattering, see Refs. 18–22 and references therein.

3 Fabrication and Verification of the SUVI Mirror Substrates

The SUVI mirror substrates are fabricated out of high quality Zerodur® manufactured by Schott. Six pairs of multilayer-coated flight mirrors were fabricated and fully calibrated. The shaping, figuring, and polishing of all the SUVI mirrors were carried out at SSG-Tinsley (Tinsley, hereafter). Herein, we focus more on the mid- and high-spatial frequency microroughness surface analyses; for more details regarding all test setups and equipment used, we refer the reader to Martínez-Galarce et al.¹⁶

3.1 Fabrication and Metrology of the SUVI Mirror Substrates

The primary mirror substrates were light-weighted with mechanical tolerances verified using a coordinate measuring machine (CMM). The secondary mirrors were not

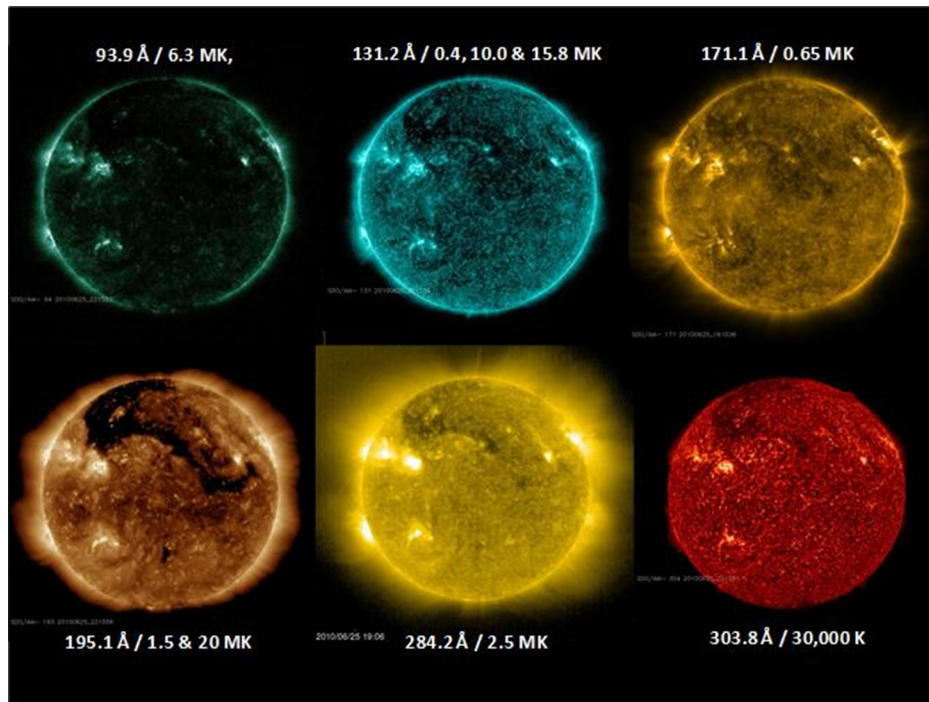


Fig. 2 Representative EUV images similar to which SUVI will record in all six of its bandpasses are shown. All but the 284.2 Å image were recorded by the AIA instrument aboard the Solar Dynamics Observatory. The 284.2 Å image is from Extreme-Ultraviolet Imaging telescope (EIT) on board the Solar Heliospheric Observatory (SoHO). These images represent a discrete range of plasma temperatures of the sun's atmosphere, from ~ 0.03 to 3 MK. During transient events (not shown), the hotter temperatures, $T > 3$ MK (up to 20 MK), are reached in flares and CMEs (see Table 2). These images show the sun on the lower end of its upward move toward solar maximum. Hence, although there are a few active regions visible in the images, the sun is mostly quiescent. The images were recorded on June 25, 2010.

light-weighted but had their dimensions verified with the CMM. The next process involved curve generation of the best fit sphere onto the substrate mirror surfaces. Conventional grinding and polishing processes were then used to prepare the optical surface for a baseline optical test, where a software null is applied. Computer controlled optical surfacing was used to deterministically converge on the figure, slope and roughness requirements.

To validate the large spatial bandwidth specifications that defined the allowed surface deviations for the SUVI optics (Table 3), a variety of metrology instruments was used. These instruments were also used for in-process feedback during fabrication of the optics and validation of the specifications once an optic was completed. The low- and mid-spatial frequencies were evaluated using phase shifting instruments: a PhaseShift MiniFiz interferometer for measuring the low-spatial frequencies and an ADE phase measuring microscope (PMM) for the mid-spatial frequencies, whereas the high-spatial frequencies were characterized using an Nanosurf Mobile S atomic force microscope (AFM).

Using full aperture interferometry, the low-spatial frequency surface errors were determined from full aperture down to 1-mm spatial periods. The final surface figure for one of the SUVI flight primary mirrors, FP1 (FP1 means flight primary mirror #1), was measured at 6328 Å to have 0.016 wv RMS (i.e., 101.2 Å, Fig. 3).

3.2 Microroughness

The surface errors at mid-spatial frequencies were characterized using the PMM. The instrument has multiple objectives available to cover spatial frequencies (1 to 1000 mm^{-1}). The

instrument uses a 1 Mpixel array camera to record images. SUVI mirrors required a 2.5 \times and a 50 \times objective, which measure $5.6 \times 5.6 \text{ mm}^2$ and $0.28 \times 0.28 \text{ mm}^2$ areas, respectively. The optical surface was sampled at 12 locations with each objective. Figure 4 shows sample PMM images from the same flight model primary mirror, FP1, shown in Fig. 3. Using Eq. (1),^{20,23} we can calculate the surface microroughness, σ_t , over the spatial frequency response of the PMM, per use of each objective; for the 2.5 \times image in Fig. 4(a), we measured a surface microroughness of 5.3 Å

Table 3 SUVI mirrors specifications: dimensions and allowed surface errors per spatial frequency ranges, referred as regions 1, 2, and 3. For spatial frequencies, $f \leq 0.25/\text{mm}$, the figure error drives the requirement.

Parameter	Value
Optics diameter	200 mm, primary; 92 mm, secondary
Surface figure	$< \lambda/20$ RMS
Surface microroughness (Region 1: $0.25/\text{mm} < f \leq 6/\text{mm}$)	$< 4.9 \text{ Å}$ RMS
Surface microroughness (Region 2: $6/\text{mm} < f \leq 700/\text{mm}$)	$< 2.5 \text{ Å}$ RMS
Surface microroughness (Region 3: $700/\text{mm} < f \leq 50,000/\text{mm}$)	$< 2.6 \text{ Å}$ RMS

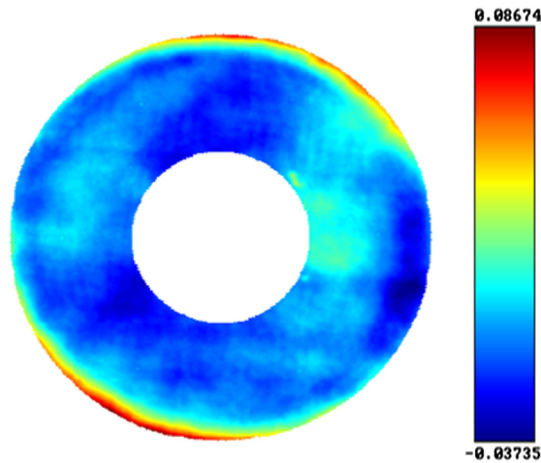


Fig. 3 Full aperture surface figure error measured over the clear aperture of the SUVI flight primary mirror, FP1 (i.e., “flight primary #1”), $\varnothing 9.5$ cm, 0.016 wv RMS. Red colored areas correspond to “peak” regions and dark blue colored areas correspond to “valleys.” Numbers are in fractions of a wv, i.e., 6328 Å.

and for the 50 \times image in Fig. 4(b) we determined a surface microroughness of 1.5 Å RMS. In Eq. (1), f is spatial frequency and $P(f)$ is the two-dimensional (2-D) power spectral density (PSD) measured by the instrument, and the integral is determined over the spatial frequency range, Δf_i ,

$$\sigma_i^2 = 2\pi \int_{\Delta f_i} P(f) f df \quad (i = 1, 2 \text{ and } 3). \quad (1)$$

Index i refers to spatial frequency regions 1, 2, and 3, respectively, as per Table 3.

To characterize the highest spatial frequencies of interest from 500/mm to 50,000/mm, the AFM was employed. Using Eq. (1), we calculated the microroughness to be 2.2 and 2.3 Å for each image shown in Figs. 5(a) and 5(b), respectively.

Lastly, using the Tinsley data gathered from the various instruments: full aperture optical tests with 100 phase averages, average of 12 locations sampled with the PMM 2.5 \times objective and the 50 \times objective, and average of 12

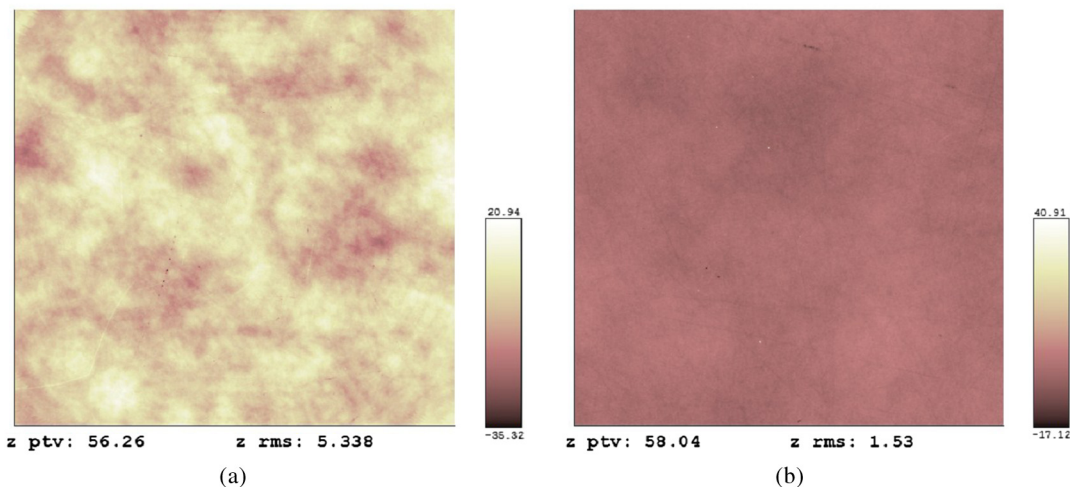


Fig. 4 (a) Phase measuring microscope (PMM) 5.6×5.6 mm² aperture measurement using 2.5 \times objective of the FP1 primary mirror with measured microroughness of 5.3 Å RMS; (b) PMM 0.28×0.28 mm² aperture measurement using a 50 \times objective for the same mirror, resulting with a measured microroughness of 1.5 Å RMS. Dark regions are lower elevations and lighter regions are higher.

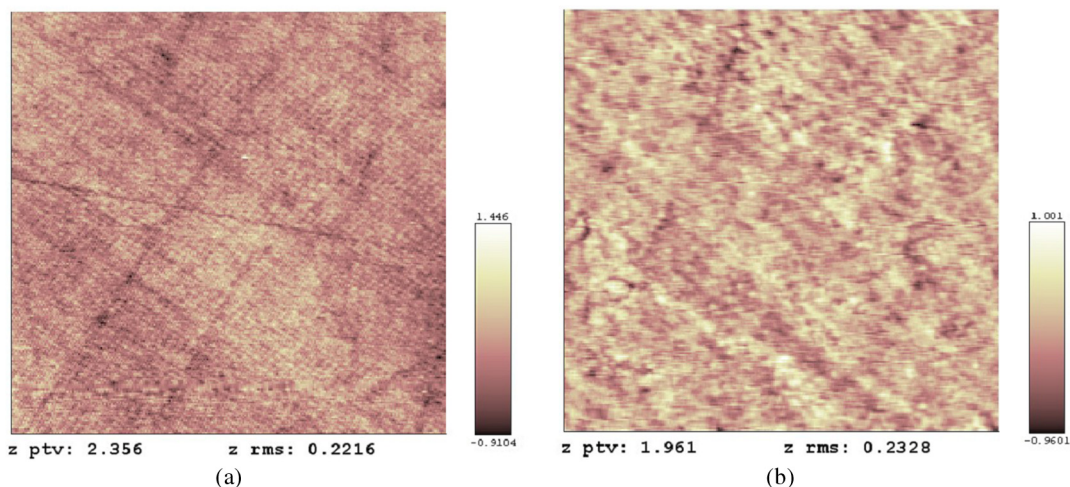


Fig. 5 (a) Atomic force microscope (AFM) 8.7×8.7 μm² aperture measurement of the FP1 primary mirror with measured microroughness of 2.2 Å RMS. (b) AFM 1.1×1.1 μm² aperture measurement of the same, with measured microroughness of 2.3 Å RMS. Dark regions are lower elevations and lighter regions are higher. Polishing marks can be seen as long streaks across the images.

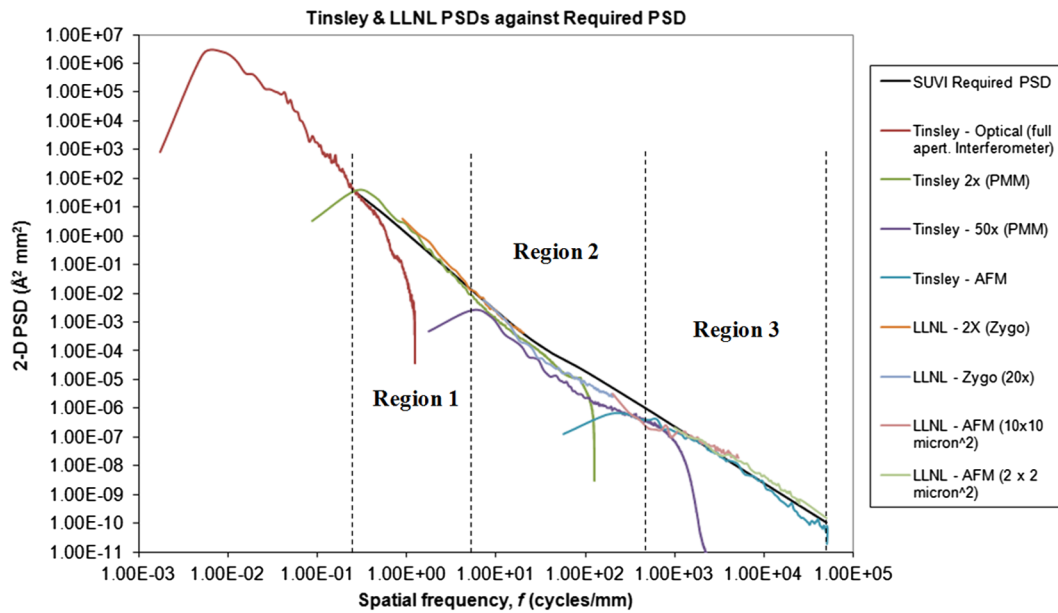


Fig. 6 Power spectral density (PSD) of FP1 measured at Tinsley and verified (prior to coating) at the Lawrence Livermore National Lab. (LLNL). PSD calculations are compared to the SUVI-required PSD. Note that for spatial frequencies, $0.007 \leq f \leq 0.25$ c/mm, the figure and slope errors drive the mirror design. Regions 1, 2, and 3 are defined in Table 3. All measured values fall within specifications and where there is overlap in spatial frequencies, the cross-instrument measurements are in relatively good agreement. The fall-off of the curves for the Tinsley full aperture, PMM, and AFM measurements are the windowing effects of those instruments and are ignored when applying Eq. (1).

locations sampled with the AFM over $8.7 \times 8.7 \mu\text{m}^2$ and $1.1 \times 1.1 \mu\text{m}^2$ scan images, a 2-D PSD was calculated over the full spatial frequency range. Figure 6 shows the complete PSD over the full spatial frequencies required for the SUVI FP1 mirror; all the SUVI mirrors were similarly measured, resulting in similar PSD curves. For comparison, we also show measurements taken at Lawrence Livermore National Laboratory (LLNL) prior to multilayer coating. High-spatial frequencies were measured at LLNL with a Digital Instruments Dimension 5000™ AFM. AFM scans of $2 \times 2 \mu\text{m}^2$ and $10 \times 10 \mu\text{m}^2$ areas were performed in various locations on the SUVI mirror substrates to determine surface microroughness. Mid-spatial frequencies were also measured at LLNL using a Zygo New View™ optical surface profiler. Scans were performed with two objective lens magnifications, 2.5 \times and 20 \times . As various instruments were used to make the PSD measurements, the locations measured were all made as close as possible to the locations measured by Tinsley. We see that the PSD calculated from the various instruments have some overlap in spatial frequencies; this inter-instrument overlap was found to be in very good agreement with each other and in comparison to the required SUVI PSD. As per the use of Eq. (1) on all the measured PSDs, in Sec. 5 we show comparison of the measured microroughness for all SUVI mirrors to the requirements listed in Table 3.

4 Multilayer Coating and EUV Calibration

4.1 Multilayer Coating

The multilayer coating performance requirements for SUVI are shown in Table 4. These specifications were determined based on the scientific requirements of the mission identified in Table 2, where the main objective of SUVI is to obtain a set of observations that cover a wide thermal measure of

the sun's dynamic atmosphere, recording observations at a cadence of a few minutes, operating over a minimum 10-year period. The multilayer coatings were fabricated using magnetron sputtering. The bilayer materials used for all SUVI EUV coatings except the one for 93.9 Å, were Molybdenum-Silicon (Mo/Si), the 93.9 Å coating was fabricated using Molybdenum-Yttrium (Mo/Y). The development of the SUVI coatings was partially based on earlier work done for the AIA multilayer mirrors,^{23,24} however, SUVI is the first EUV solar telescope fabricated with six different multilayer coatings on a single optic.

Table 4 The channel peak wavelength corresponds to the primary solar emission line of interest that falls within the SUVI bandpass, where the width (full-width at half maximum) is defined by the corresponding value in the rightmost column. The corresponding multilayer peak reflectivity refers to the minimum requirement at the targeted solar emission line wavelength to assure instrument throughput performance over the full mission lifetime.

EUV channel peak wavelength (Å; corresponding to principal solar emission line)	Multilayer peak reflectivity specification (%)	Multilayer bandwidth specification (Å)
93.9 ± 0.6 (Fe XIII)	≥ 21.4	≤ 2.0
131.2 ± 1.3 (Fe XX & XXIII)	≥ 51.3	≤ 6.0
171.1 ± 2.1 (Fe IX)	≥ 34.2	≤ 8.5
195.1 ± 2.8 (Fe XII)	≥ 25.7	≤ 11.0
284.2 ± 6.3 (Fe XV)	≥ 17.1	≤ 25.0
303.8 ± 6.3 (He II)	≥ 17.1	≤ 25.0

Prior to multilayer deposition, all mirrors were cleaned at LLNL using a customized process for optical substrates.²⁵ Afterward, the 131.2 and 171.1 Å multilayer coatings were deposited at LLNL and then the mirrors were shipped to Reflective X-ray Optics, LLC (RXO), where the coatings for the other four wavelengths, 93.9, 195.1, 284.2 and 303.8 Å, were deposited (see Refs. 26 and 27 for descriptions of their deposition systems). Depending on the chamber used, the background pressure was held in the range of $\sim 10^{-7}$ to 10^{-6} Torr and the sputter gas (Ar) pressure was maintained at ~ 1 to 2 mTorr during multilayer deposition. The design parameters of the multilayer coatings are summarized in Table 5. In the case of the high film stress coatings, a precoating of 100 Å Cr was deposited to mitigate the risk of any film stress-driven adhesion failures. All six coatings were deposited on each mirror as 60-deg “pie wedge” segments as seen in Fig. 7. For program risk mitigation, two multilayer witness samples (MLWS), each deposited on a $\sim 2 \times 2$ cm² Si wafer substrate, were also simultaneously coated with each SUVI mirror coating segment. A total of

144 MLWS were fabricated. The MLWS are stored with the flight mirrors up to the time of the mirror’s integration into a telescope and can be used to monitor the performance of the coatings over the lifetime of the instrument.

4.2 EUV Calibration

Calibration of the SUVI optics consists of EUV reflectivity measurements that were carried out on beamline 6.3.2. at the advanced light source (ALS) synchrotron facility of the Lawrence Berkeley National Laboratory. The characteristics of beamline 6.3.2. and its reflectometer have been described in detail by Gullikson et al.²⁸ A schematic drawing of the beamline facility is shown in Fig. 8. Wavelength calibration is based on the $L_{2,3}$ absorption edge of an appropriate filter (Si or Al, in this work) with a relative accuracy of 0.011% rms and can be determined with 0.007% repeatability. Curved optics of up to 300 mm in diameter can be mapped in this facility. The reflectometer sample stage shown in Fig. 9 allows motion of the optic in three dimensions

Table 5 Multilayer coating design parameters for SUVI.

Wavelength (Å)	93.9	131.2	171.1	195.1	284.2	303.8
Multilayer materials	Mo/Y	Mo/Si	Mo/Si	Mo/Si	Mo/Si	Mo/Si
d (bi-layer thickness, Å)	47.80	67.15	88.35	102.00	152.50	165.00
N (number of bi-layers)	120	50	40	40	20	20
$\Gamma(d_1/d_{tot})$	0.35	0.36	0.175	0.15	0.15	0.15
Capping layer	16.3 Å Mo	35.0 Å Si	35.0 Å Si	35.0 Å Si	30.0 Å Si	30.0 Å Si
Chromium adhesion layer	No	No	No	100 Å	100 Å	100 Å

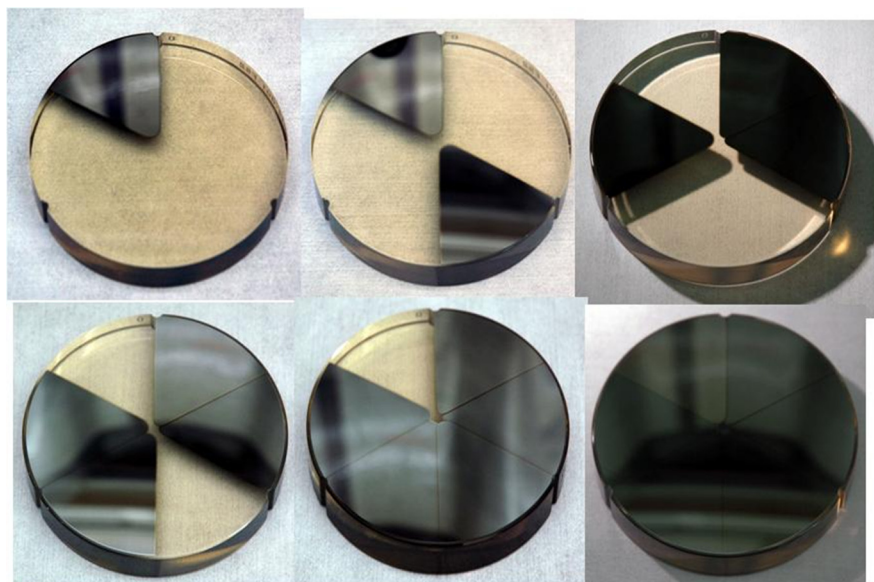


Fig. 7 The SUVI secondary mirror, FS1. Each of the six multilayer coatings, seen here as “pie” segments, was successively deposited in a similar fashion on each mirror. An aperture selector will be used in the SUVI instrument to allow illumination of the specific coating segment needed to pass the desired EUV light.

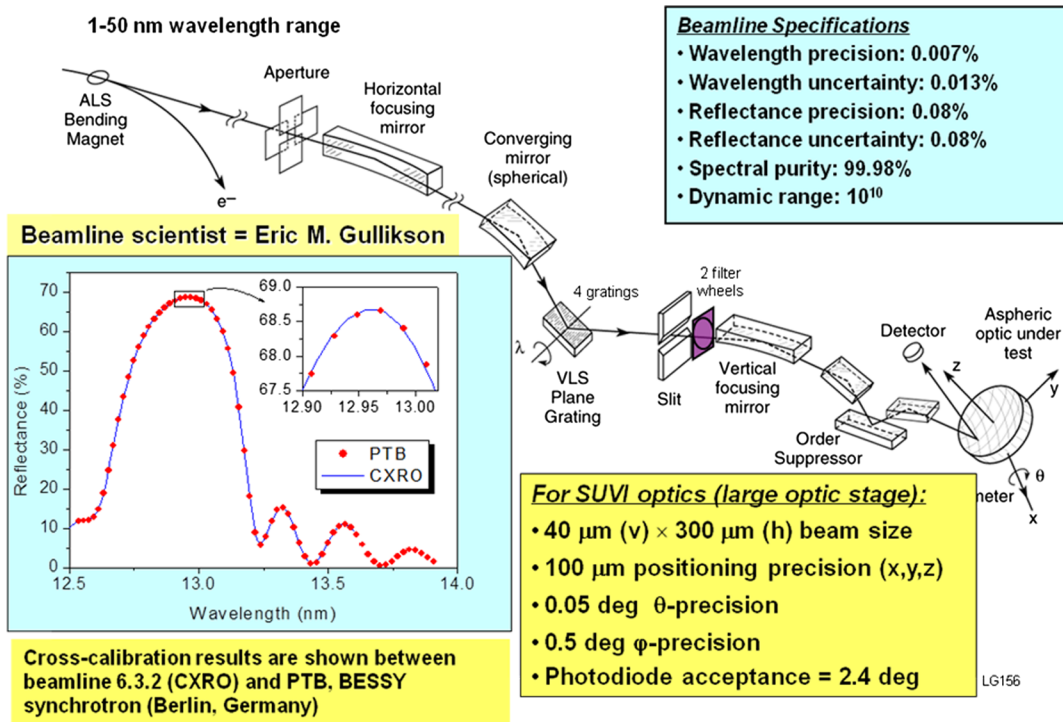


Fig. 8 Schematic drawing of beamline 6.3.2. and outline of its capabilities.

(x , y , and z), and rotation of the incidence angle, tilt, and azimuth angle of the optic.

The available detectors include a selection of photodiodes and a CCD camera (the latter used for sample alignment). Once the optic is aligned, custom-designed software allows the operator to program all EUV wavelength scan measurements (i.e., scans taken at multiple locations on the mirror surface) without any manual input needed in-between scans. Alignment is verified and adjusted, if necessary, separately for each SUVI coating segment (i.e., wavelength channel). The signal was collected on a Si photodiode detector with a $10 \times 10 \text{ mm}^2$ active area with an acceptance angle

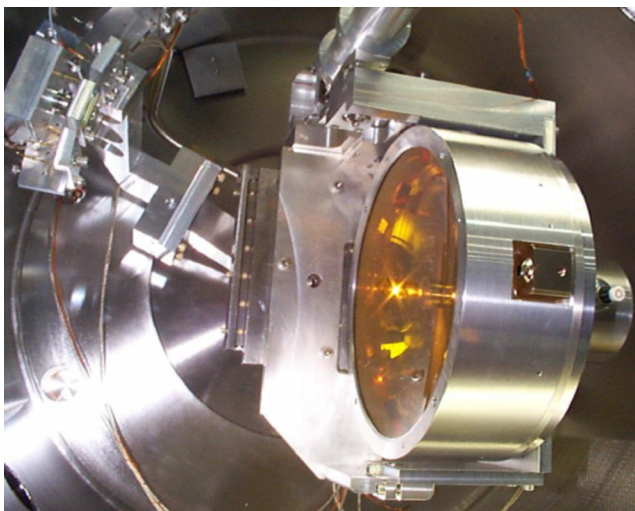


Fig. 9 Interior of reflectometer chamber at ALS beamline 6.3.2. is shown with a mounted optic (not SUVI). The detector arm is also shown (top left).

of 2.4 deg. For the reflectivities measured, the peak-to-valley relative accuracy was in the range 0.4% to 1%, determined by the Si photodiode's spatial uniformity in each wavelength range. The total absolute uncertainty across all EUV channels on all mirrors ranged between 0.02% and 0.71%, but on average was $\sim 0.24\%$ (see Table 6).

During the EUV reflectivity measurements, the incidence angle (from the normal direction) for the SUVI primary mirror was fixed at $\theta_i = 3.1$ deg which is the SUVI primary flight mirror incidence angle at a radius, $r = 76$ mm, (the weighted center of the SUVI primary mirror's clear aperture, or CA). Similarly, the incidence angle for the secondary mirror was fixed at $\theta_i = 4.4$ deg, which is the secondary mirror's incidence angle in the SUVI instrument at $r = 30$ mm, the weighted center of the secondary mirror CA. Due to geometrical constraints, the smallest angle that can be measured at the ALS reflectometer is about 3 deg. The coating segment geometry of the EUV reflectivity scans is shown in Fig. 10. Each coating segment of each mirror was measured successively at 30 locations for the primary mirror and 47 locations for the secondary mirror, across the CA of the coating, as a function of radius and azimuth angle, (r , φ). A sample of the measured EUV reflectivity results is shown in Fig. 11. It is evident from the curves shown that there is more variability in the EUV reflectivity seen for the secondary mirror, FS1 (FS1 means flight secondary mirror #1) than there is for FP1. This variability is due to "shadowing," i.e. the effect of the hardware mask (installed on top of the mirror during multilayer deposition) on the segment being coated. Shadowing also includes the "over-spray" between adjacent coatings, as the mask is shifted from one sector to another to deposit each successive coating. This is markedly the case for all the secondary mirrors in comparison to the primary mirrors. The shadowing effect is more pronounced in the secondary mirrors due to the smaller geometry and closer

Table 6 The area-weighted average reflectivities for all the SUVI flight mirrors, FP*n* and FS*n*, where *n* is for mirror number, $n = 1, \dots, 6$, respectively, are shown. “P” is for primary mirror and “S” is for secondary mirror. Area-weighted reflectivity is per Eq. (2); “ALS Meas. absolute uncertainty” is the single location measurement uncertainty per EUV channel; and the “weighted uncertainty” is the total RSS value of the latter uncertainty with the area-weighted uncertainty calculated via Eq. (3). Skewness and kurtosis are shown to indicate “Gaussian-likeness.”

		FP1					FS1				
EUV Channel (Angstrom)	Required Reflectivity (%)	Area-weighted avg. reflectivity (%)	ALS Meas. Absolute Uncertainty (± 1 -sigma)	Weighted Uncertainty (± 1 -sigma)*	Skewness Measure of Data	Kurtosis (compared to normal dist.)	Area-weighted avg. reflectivity (%)	ALS Meas. Absolute Uncertainty (± 1 -sigma)	Weighted Uncertainty (± 1 -sigma)*	Skewness Measure of Data	Kurtosis (compared to normal dist.)
93.9	21.4%	26.18%	0.13%	1.51%	-0.83	0.30	24.82%	0.06%	7.17%	-1.74	1.92
131.2	51.3%	63.65%	0.13%	0.36%	-1.33	2.14	61.61%	0.13%	6.89%	-3.02	8.55
171.1	34.2%	46.02%	0.09%	0.21%	-0.91	-0.50	45.67%	0.10%	1.28%	-5.01	28.60
195.1	25.7%	35.22%	0.07%	0.79%	-2.25	4.04	33.15%	0.08%	6.60%	-2.32	4.65
284.2	17.1%	23.78%	0.06%	0.44%	-0.46	-0.93	22.52%	0.07%	3.53%	-2.43	5.42
303.8	17.1%	22.46%	0.05%	0.23%	-0.99	0.12	21.58%	0.08%	2.97%	-3.62	12.88
		FP2					FS2				
EUV Channel (Angstrom)	Required Reflectivity (%)	Area-weighted avg. reflectivity (%)	ALS Meas. Absolute Uncertainty (± 1 -sigma)	Weighted Uncertainty (± 1 -sigma)*	Skewness Measure of Data	Kurtosis (compared to normal dist.)	Area-weighted avg. reflectivity (%)	ALS Meas. Absolute Uncertainty (± 1 -sigma)	Weighted Uncertainty (± 1 -sigma)*	Skewness Measure of Data	Kurtosis (compared to normal dist.)
93.9	21.4%	28.69%	0.69%	3.86%	-1.93	1.33	27.41%	0.13%	7.38%	-1.79	2.16
131.2	51.3%	64.20%	0.32%	0.45%	-0.03	-1.41	58.08%	0.29%	11.06%	-2.47	5.32
171.1	34.2%	47.52%	0.24%	0.33%	-0.16	1.25	43.73%	0.22%	7.81%	-2.50	8.65
195.1	25.7%	31.75%	0.08%	2.19%	-2.18	3.13	31.90%	0.03%	5.80%	-2.36	4.55
284.2	17.1%	24.25%	0.17%	0.22%	0.94	0.22	22.04%	0.15%	3.26%	-2.38	4.87
303.8	17.1%	22.31%	0.16%	0.20%	0.73	-0.28	21.56%	0.15%	2.50%	-2.38	4.43
		FP3					FS3				
EUV Channel (Angstrom)	Required Reflectivity (%)	Area-weighted avg. reflectivity (%)	ALS Meas. Absolute Uncertainty (± 1 -sigma)	Weighted Uncertainty (± 1 -sigma)*	Skewness Measure of Data	Kurtosis (compared to normal dist.)	Area-weighted avg. reflectivity (%)	ALS Meas. Absolute Uncertainty (± 1 -sigma)	Weighted Uncertainty (± 1 -sigma)*	Skewness Measure of Data	Kurtosis (compared to normal dist.)
93.9	21.4%	32.49%	0.20%	0.24%	0.32	-0.61	24.52%	0.07%	6.71%	-1.54	1.42
131.2	51.3%	66.15%	0.33%	0.36%	-0.71	-0.38	61.71%	0.17%	6.08%	-3.84	14.20
171.1	34.2%	48.33%	0.24%	0.25%	-0.39	-1.37	46.22%	0.23%	5.42%	-3.82	13.73
195.1	25.7%	36.15%	0.18%	1.27%	-2.26	3.66	33.02%	0.10%	4.72%	-3.04	9.23
284.2	17.1%	24.15%	0.34%	0.40%	-1.47	1.34	21.93%	0.17%	3.08%	-3.09	9.49
303.8	17.1%	22.64%	0.32%	0.43%	-0.52	-0.70	21.03%	0.15%	4.56%	-2.01	2.30
		FP4					FS4				
EUV Channel (Angstrom)	"Spec" Reflectivity (%)	Area-weighted avg. reflectivity (%)	ALS Meas. Absolute Uncertainty (± 1 -sigma)	Weighted Uncertainty (± 1 -sigma)*	Skewness Measure of Data	Kurtosis (compared to normal dist.)	Area-weighted avg. reflectivity (%)	ALS Meas. Absolute Uncertainty (± 1 -sigma)	Weighted Uncertainty (± 1 -sigma)*	Skewness Measure of Data	Kurtosis (compared to normal dist.)
93.9	21.4%	31.10%	0.17%	0.37%	-1.80	3.75	23.70%	0.10%	5.29%	-1.88	3.44
131.2	51.3%	63.97%	0.32%	0.47%	1.13	0.94	61.87%	0.31%	6.04%	-4.33	22.09
171.1	34.2%	46.68%	0.23%	0.26%	-0.79	-0.64	46.51%	0.23%	4.53%	-3.87	15.19
195.1	25.7%	34.94%	0.25%	0.65%	-2.10	3.55	32.32%	0.19%	5.41%	-2.38	5.32
284.2	17.1%	25.28%	0.58%	0.61%	-0.86	0.02	23.48%	0.59%	4.70%	-2.81	7.17
303.8	17.1%	24.18%	0.56%	0.61%	-1.18	1.13	22.09%	0.55%	5.30%	-1.84	1.65
		FP5					FS5				
EUV Channel (Angstrom)	"Spec" Reflectivity (%)	Area-weighted avg. reflectivity (%)	ALS Meas. Absolute Uncertainty (± 1 -sigma)	Weighted Uncertainty (± 1 -sigma)*	Skewness Measure of Data	Kurtosis (compared to normal dist.)	Area-weighted avg. reflectivity (%)	ALS Meas. Absolute Uncertainty (± 1 -sigma)	Weighted Uncertainty (± 1 -sigma)*	Skewness Measure of Data	Kurtosis (compared to normal dist.)
93.9	21.4%	28.39%	0.56%	3.62%	-1.83	2.79	24.03%	0.12%	5.93%	-1.76	2.63
131.2	51.3%	65.16%	0.33%	0.40%	-0.29	-0.23	61.26%	0.32%	7.31%	-2.86	8.58
171.1	34.2%	48.09%	0.24%	0.27%	-0.05	-1.21	46.08%	0.23%	5.78%	-3.12	10.95
195.1	25.7%	33.10%	0.23%	4.53%	-1.77	1.98	31.87%	0.19%	4.04%	-2.92	8.46
284.2	17.1%	26.29%	0.09%	0.12%	-0.10	0.33	23.20%	0.53%	5.01%	-2.71	6.52
303.8	17.1%	24.77%	0.09%	0.19%	-0.21	-0.78	21.57%	0.50%	5.65%	-1.81	1.63
		FP6					FS6				
EUV Channel (Angstrom)	"Spec" Reflectivity (%)	Area-weighted avg. reflectivity (%)	ALS Meas. Absolute Uncertainty (± 1 -sigma)	Weighted Uncertainty (± 1 -sigma)*	Skewness Measure of Data	Kurtosis (compared to normal dist.)	Area-weighted avg. reflectivity (%)	ALS Meas. Absolute Uncertainty (± 1 -sigma)	Weighted Uncertainty (± 1 -sigma)*	Skewness Measure of Data	Kurtosis (compared to normal dist.)
93.9	21.4%	28.62%	0.57%	1.78%	-0.41	-0.92	23.13%	0.02%	6.73%	-1.57	1.48
131.2	51.3%	64.27%	0.33%	0.37%	0.32	-0.58	57.61%	0.31%	10.27%	-2.62	6.78
171.1	34.2%	47.17%	0.33%	0.38%	-0.23	-1.96	43.19%	0.22%	7.38%	-2.42	5.20
195.1	25.7%	34.25%	0.29%	2.07%	-1.81	2.26	30.24%	0.18%	5.92%	-1.81	2.71
284.2	17.1%	26.10%	0.71%	0.78%	-0.59	-0.63	23.12%	0.07%	4.16%	-2.58	5.99
303.8	17.1%	25.04%	0.68%	0.68%	-0.64	-0.19	22.15%	0.07%	4.92%	-1.94	2.11

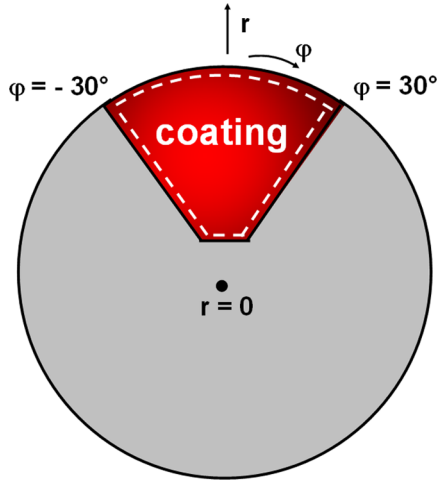


Fig. 10 Schematic drawing of a coating on a mirror where the red region represents one EUV channel (e.g., the 195.1 Å channel) corresponding to one (of six) multilayer-coated sector(s). Region bounded by dashes is the clear aperture (CA) of the coated sector and the region actually measured at EUV wavelengths. Polar coordinates are used to mark the geometry of each sector.

proximity of the side-by-side CA of the multilayer coatings, designed with only a 2-mm separation at their edges, while for the primary mirrors, the separation between the edges of their adjacent CA is 23 mm. Each curve shown in Figs. 11(e) and 11(f) represents a reflectivity versus wavelength scan at one location on the mirror for both mirrors; the measurements are accurate to within 0.13% absolute uncertainty (see Table 6). For FS1, however, we see that the degradation at the coated segment boundaries adds to the weighted uncertainty, 6.89%, shown in Tables 6 and 7. But for FP1, the calculated weighted uncertainty, 0.36%, is nearer the ALS measured value of 0.13%, meaning that there is less reflectivity variation across the CA of the coating, and this is supported by the data shown in Fig. 11.

5 Analysis and Discussion

The ALS measured absolute uncertainty reported in Table 6 is the single measurement uncertainty of a measurement made at a single spatial point (i.e., one location) on the SUVI mirror at a specific wavelength, λ_i . To accurately measure the overall throughput of the instrument, we measured the total reflectivity over the CA of the coated area, taking measurements on 30 (primary) and on 47 (secondary) locations across the CA of each coating on each mirror. To gauge the uncertainty of calculating the entire coated segment's reflectivity, we weighed each individual-location measurement by the subarea it is associated with on the coated segment. The main reasons why a number of locations are measured are to account for peak wavelength variations across the coated CA due to multilayer thickness nonuniformities and peak reflectivity variations due to multilayer thickness and substrate roughness variations. Furthermore, there are variations due to coating overlap at the coated segment boundaries. It is the undersampled part of these variations that contribute to the variability seen in each location measured. Hence, these variations are grouped together as a single uncertainty. Using all the single-location measurements, predefined over the CA of the coated sector, the

total reflectivity is calculated as a weighted average over the CA, given by

$$\langle \rho_{m,\lambda_i} \rangle = \left(\sum_{q=1}^K \rho_{m,\lambda_i,q} a_{m,\lambda_i,q} \right) / A_{m,\lambda_i,\text{total}}, \quad (2)$$

where $A_{m,\lambda_i,\text{total}} = \sum_{q=1}^K a_{m,\lambda_i,q}$, the CA of the coating; $\rho_{m,\lambda_i,q}$ is the reflectivity measured at wavelength λ_i , at the predefined location q on the coated subsector, measured at a specified polar coordinate location (Fig. 10); $a_{m,\lambda_i,q}$ is the subsector area of that polar coordinate location, corresponding to where the measurement was made, and K is the total number of locations measured over the entire coated CA. Subscript $m (= 1, \dots, 12)$ is the mirror identification index.

Because the individual-location measurements are very accurate (on average measured to $\sim 0.24\%$, absolute accuracy), the variability in reflectivity measured across the coated CA that is $> 0.24\%$ of the average value calculated in Eq. (2) is a real effect that is inherent in the coating. This variability adds to the uncertainty of estimating the weighted average reflectivity in Eq. (2). Hence, we must also estimate the uncertainty due to spatial variation of the reflectivity by calculating the subsector, area-weighted deviation, $\sigma_{m,\lambda_i,q}$, given by

$$\sigma_{m,\lambda_i,q} = \sqrt{\frac{1}{A_{m,\lambda_i,\text{tot}}} \sum_{q=1}^K a_{m,\lambda_i,q} (\langle \rho_{m,\lambda_i} \rangle - \rho_{m,\lambda_i,q})^2}. \quad (3)$$

Next, we calculate the root-sum-square of this value with the ALS absolute measurement uncertainty to get the total weighted uncertainty reported in Table 6. Because of the non-Gaussian distribution of the measurements, Eq. (3) overestimates the uncertainty in the weighted average due to the finite number of measurements and, $\rho_{m,\lambda_i,q}$, made in each coating. It would be more useful to calculate the variation by applying a 2-D “best fit” surface to the K measurements taken across the CA and then calculating the deviation of the K measurements from this surface. But to do this with reasonable accuracy requires taking many more measurements across the CA to more accurately map the 2-D surface fit, particularly near the edges of the CA. It is clear that as the number of measurements K , approaches infinity, the total uncertainty in determining the weighted average would converge to the individual measurement uncertainty of $\sim 0.24\%$ (i.e., the average absolute uncertainty reported in Sec. 4). But also, the weighted average value would converge to a value slightly different than that reported in Table 6. Due to programmatic constraints in time and cost, this was not performed.

We note that the degradation in reflectivity after calibration is due primarily to partial oxidation of the top layer of the multilayer coating. Degradation due to contamination will be minimum due to strict handling procedures imposed on the program requiring the coated optics be maintained under constant nitrogen purge in a dry box located inside a “Class 1000” clean room (ISO 14644-1 standards). However, oxidation of the top layer of the multilayer coatings will increase each time they are exposed to air, where nominally, the majority of this effect occurs mostly within days to a few weeks' time of exposure and then gradually plateaus. After being coated, the mirrors are exposed to

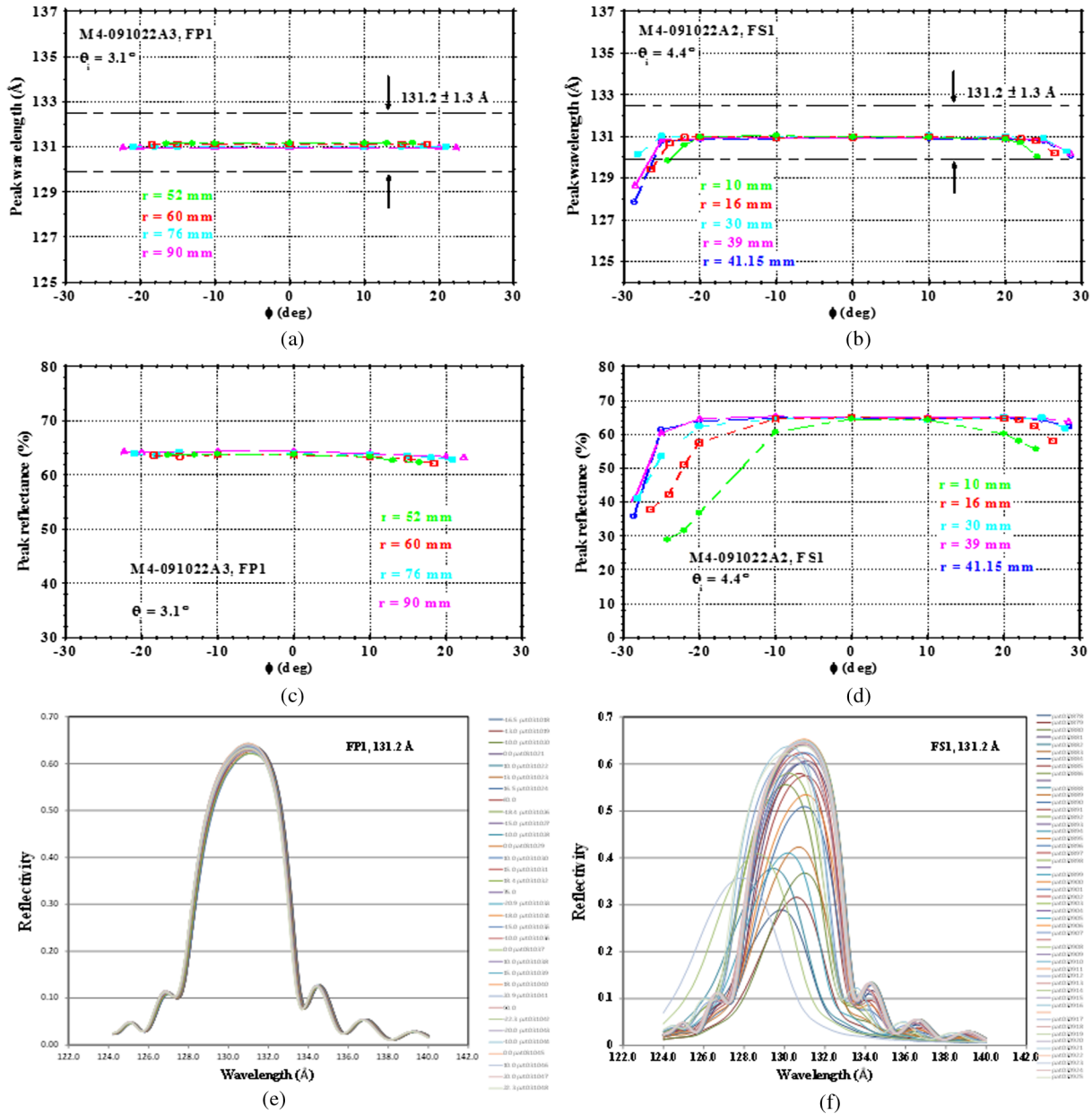


Fig. 11 Panels (a), (c) and (e) show EUV measurements taken for the 131.2 Å channel of flight primary mirror, FP1. Panels (b), (d) and (f) show EUV measurements taken for the 131.2 Å channel of flight secondary mirror, FS1. Panels (a) and (b) are the peak wavelength response plotted over the CA at 50 and 37 locations (primary and secondary, respectively) mapped in polar coordinates, see Fig. 10. The dashed lines in (a) and (b) represent the specified tolerance for the peak wavelength of each SUVI multilayer coating shown as the “±” values in the left column in Table 4. Panels (c) and (d) show the peak reflectivity measured near 131.2 Å for each location measured on each mirror. Panels (e) and (f) show the reflectivity versus wavelength curves measured on each location across the CA of FP1 and FS1, respectively.

air while undergoing visual inspection, calibration measurements, and integration and testing in the SUVI instrument. But within a few weeks of being multilayer coated, the mirror is placed in a dry box with continual nitrogen purge. During the course of SUVI integration and testing, exposure will also occur during short periods involving comprehensive performance test procedures that will expose the optics to air. The uncertainty due to this effect is estimated to be about 5% from the time the coating is initially measured to the time SUVI first becomes operational on orbit. To more accurately account for this degradation, the MLWS that were multilayer coated simultaneously with the flight mirrors are also

measured at the time the flight mirrors are calibrated and then again at 1 year postcoating to measure degradation in performance, if any.

Table 6 shows the area-weighted average reflectivity of each coating on each mirror. The corresponding area-weighted, $1 - \sigma$ uncertainties of these measurements, are also shown. The designation “P” in FP1, FP2, etc., refers to the primary mirror, whereas “S” in FS1, FS2, etc., refers to the secondary mirror; a total of six pairs of flight-quality primary and secondary mirrors have been fabricated. For reference, we also include the absolute uncertainty measured at a single location (i.e., ALS uncertainty), as well as the

Table 7 Microroughness measurements taken at Tinsley and at LLNL are shown in comparison with at-wavelength, area-weighted, averaged EUV reflectivities that were measured at the ALS compared with required throughput values (the latter does not incorporate end-of-life degradation).

Mirror	Measured RMS Microroughness $\pm 1-\sigma$ uncertainty (in Å)			Area-weighted Averages of Measured Reflectivities (%) $\pm 1-\sigma$ uncertainties**							
	(SSG-Tinsley reported)			(LLNL reported)		(calculated from ALS measurements reported by LLNL)					
	PSD Region 1: 0.25-6 cycles/mm	PSD Region 2: 6-700 cycles/mm	PSD Region 3: 700 - 50,000 cycles/mm	Region 2: 700 cycles/mm	Region 3: 700 - 50,000 cycles/mm	93.9 Å	131.2 Å	171.1 Å	195.1 Å	284.2 Å	303.8 Å
SPEC Req't =>	≤ 2.5	≤ 2.5	≤ 2.6	≤ 2.5	≤ 2.6	≥ 25.0	≥ 60.0	≥ 40.0	≥ 30.0	≥ 20.0	≥ 20.0
FP1	4.7 \pm 0.1	1.4 \pm 0.1	2.3 \pm 0.3	2.4 \pm 0.9	3.2 \pm 1.3*	26.2 \pm 1.5	63.7 \pm 0.4	46.0 \pm 0.2	35.2 \pm 0.8	23.8 \pm 0.4	22.5 \pm 0.2
FP2	4.1 \pm 0.2	2.0 \pm 0.4	2.4 \pm 0.3	2.5 \pm 0.4	2.9 \pm 0.8	28.7 \pm 3.9 [§]	64.2 \pm 0.5	47.5 \pm 0.3	31.8 \pm 2.2 [§]	24.2 \pm 0.2	22.3 \pm 0.2
FP3	4.0 \pm 0.1	1.2 \pm 0.1	1.7 \pm 0.4	N/M	2.4 \pm 0.2	32.5 \pm 0.2	66.2 \pm 0.4	48.3 \pm 0.3	36.2 \pm 1.3 [§]	24.2 \pm 0.4	22.6 \pm 0.4
FP4	4.5 \pm 0.2	2.1 \pm 0.2	2.6 \pm 0.3	N/M	3.3 \pm 0.1*	31.0 \pm 0.4	64.0 \pm 0.5	46.7 \pm 0.3	34.9 \pm 0.6 [§]	25.3 \pm 0.6	24.2 \pm 0.6
FP5	4.9 \pm 0.3	2.1 \pm 0.2	1.9 \pm 0.3	N/M	2.9 \pm 1.2*	28.4 \pm 3.6 [§]	65.2 \pm 0.4	48.1 \pm 0.3	33.1 \pm 4.5 [§]	26.3 \pm 0.1	24.8 \pm 0.2
FP6	4.5 \pm 0.2	2.2 \pm 0.1	2.4 \pm 0.3	N/M	3.0 \pm 0.2	28.6 \pm 1.8	64.3 \pm 0.4	47.2 \pm 0.4	34.3 \pm 2.1 [§]	26.1 \pm 0.8	25.0 \pm 0.7
FS1	4.6 \pm 0.3	1.8 \pm 0.2	1.4 \pm 0.2	2.1 \pm 0.4	1.4 \pm 0.5	24.8 \pm 7.2 [§]	61.6 \pm 6.9 [§]	45.7 \pm 1.3 [§]	33.2 \pm 6.6 [§]	22.5 \pm 3.5 [§]	21.6 \pm 3.0 [§]
FS2	4.7 \pm 0.1	1.8 \pm 0.2	2.0 \pm 0.3	N/M	2.5 \pm 0.3	27.4 \pm 7.4 [§]	58.1 \pm 11.1 [§]	43.7 \pm 7.8 [§]	31.9 \pm 5.8 [§]	22.0 \pm 3.3 [§]	21.6 \pm 2.5 [§]
FS3	5.1 \pm 0.1	1.4 \pm 0.1	2.2 \pm 0.3	N/M	2.2 \pm 0.4	24.5 \pm 6.7 [§]	61.7 \pm 6.1 [§]	46.2 \pm 5.4 [§]	33.0 \pm 4.7 [§]	21.9 \pm 3.1 [§]	21.0 \pm 4.6 [§]
FS4	4.3 \pm 0.1	1.6 \pm 0.2	2.0 \pm 0.3	N/M	2.0 \pm 0.4	23.7 \pm 5.3 [§]	61.9 \pm 6.0 [§]	46.4 \pm 4.5 [§]	32.3 \pm 5.4 [§]	23.5 \pm 4.7 [§]	22.1 \pm 5.3 [§]
FS5	4.6 \pm 0.1	2.0 \pm 0.2	1.9 \pm 0.3	N/M	1.9 \pm 0.1	24.0 \pm 5.9 [§]	61.3 \pm 7.3 [§]	46.1 \pm 5.8 [§]	31.9 \pm 4.0 [§]	23.2 \pm 5.0 [§]	21.6 \pm 5.7 [§]
FS6	4.4 \pm 0.1	2.0 \pm 0.2	2.4 \pm 0.3	N/M	3.6 \pm 1.1*	23.1 \pm 6.7 [§]	57.6 \pm 10.3 [§]	43.2 \pm 7.4 [§]	30.2 \pm 5.9 [§]	23.1 \pm 4.2 [§]	22.1 \pm 4.9 [§]

N/M = Not measured

* based on 2 measurements

** clear aperture measured over more than 40 locations

& Data has high skewness & kurtosis, so

uncertainty is an over-estimate, by as

much as a factor 2

area-weighted skewness and kurtosis measures of the data to estimate the non-Gaussian behavior of the dataset. All values shown are referred to as “initial measurement” values, which refer to the first reflectivity measurement taken in the mission timeline. Degradation effects leading to the beginning-of-life (i.e., when “first light” is seen) were discussed previously; degradation effects leading to end-of-life (i.e., the end of its mission) operation will be monitored via cross-calibration with its “sister” instrument on board GOES R+, EXIS.²⁹

Table 7 shows the microroughness measurements taken prior to multilayer coating of the optics. Measurements were carried out at metrology facilities located at Tinsley and LLNL, but using different instrumentation and setups, as described in Sec. 3 (see Ref. 16 for more details). We note that fewer “spot” measurements were taken across the optic at LLNL than at Tinsley: i.e., two to five measurement locations in contrast to a dozen locations, respectively, thus yielding better statistics for the Tinsley measurements. We note further that each “spot” measurement is taken over an area of $\sim 1.1 \times 1.1 \mu\text{m}^2$ and $8.7 \times 8.7 \mu\text{m}^2$ which is a minute fraction (i.e., sample) of the total clear aperture, corresponding to $\sim 10^{-6}\%$ to $10^{-9}\%$. Due to the complexity, time spent, risk in handling and cost of performing these measurements, carrying out more measurements was not possible. Nonetheless, the region 3 measurements listed in the table all lie within measurement uncertainties.

Last, in Fig. 12, we show all the area weighted, in-band reflectivity curves determined for each EUV channel of each SUVI flight mirror. We note that the secondary mirrors perform lower than the primary mirrors, which as previously mentioned, is due to shadowing effects and are a known and expected phenomenon given the tighter geometry and coating design requirements imposed on the secondary mirrors, compared to those of the primary mirrors. This relatively lower reflectivity, however, will not detrimentally

affect SUVI’s predicted throughput performance, as there is ample margin. Overall, the measured variation in EUV performance of each channel for all the mirrors demonstrates that the process imposed and followed on the SUVI program to design, fabricate and test these 12 mirrors was well executed, as all design and performance requirements were fully met.

6 Summary

SUVI is an EUV imaging telescope that will replace the solar X-ray monitoring telescopes, Solar X-ray Imager (SXI), that are on board the current fleet of GOES satellites. Operable in six narrow EUV bandpasses, SUVI will provide high fidelity data to observe, measure, and monitor the solar atmosphere. SUVI is the first EUV solar telescope whose multilayer-coated mirrors are a novel design in that the multilayer coatings on each mirror are segmented into six individual coated regions, each coated sector designed to reflect light in one of six EUV bandpasses centered at 93.9, 131.2, 171.1, 195.1, 284.2 and 303.8 Å. By the use of an aperture selector and one of several thin-film metallic filters, compared to SXI, SUVI will record EUV spectroheliograms with comparable imaging performance ($5 \times 5 \text{ arc sec}^2$) but higher temporal resolution (cadence of a few minutes) and broader thermal coverage of the solar atmosphere ($\sim 50,000 \text{ K}$ to $\sim 20 \text{ MK}$), operating over a 10-year mission lifetime.

Given the projected mission lifetime, users of SUVI will require accurate knowledge of its overall optical performance throughout the mission, in terms of throughput and imaging resolution. The detailed microroughness calculations presented herein, determined from PSD measurement analyses, coupled with the detailed EUV reflectivity measurements taken of all the flight optics (and witness samples), allow for an accurate prediction of SUVI’s beginning-of-life imaging and throughput performance as well as monitoring of this performance over its operational lifetime. Compared

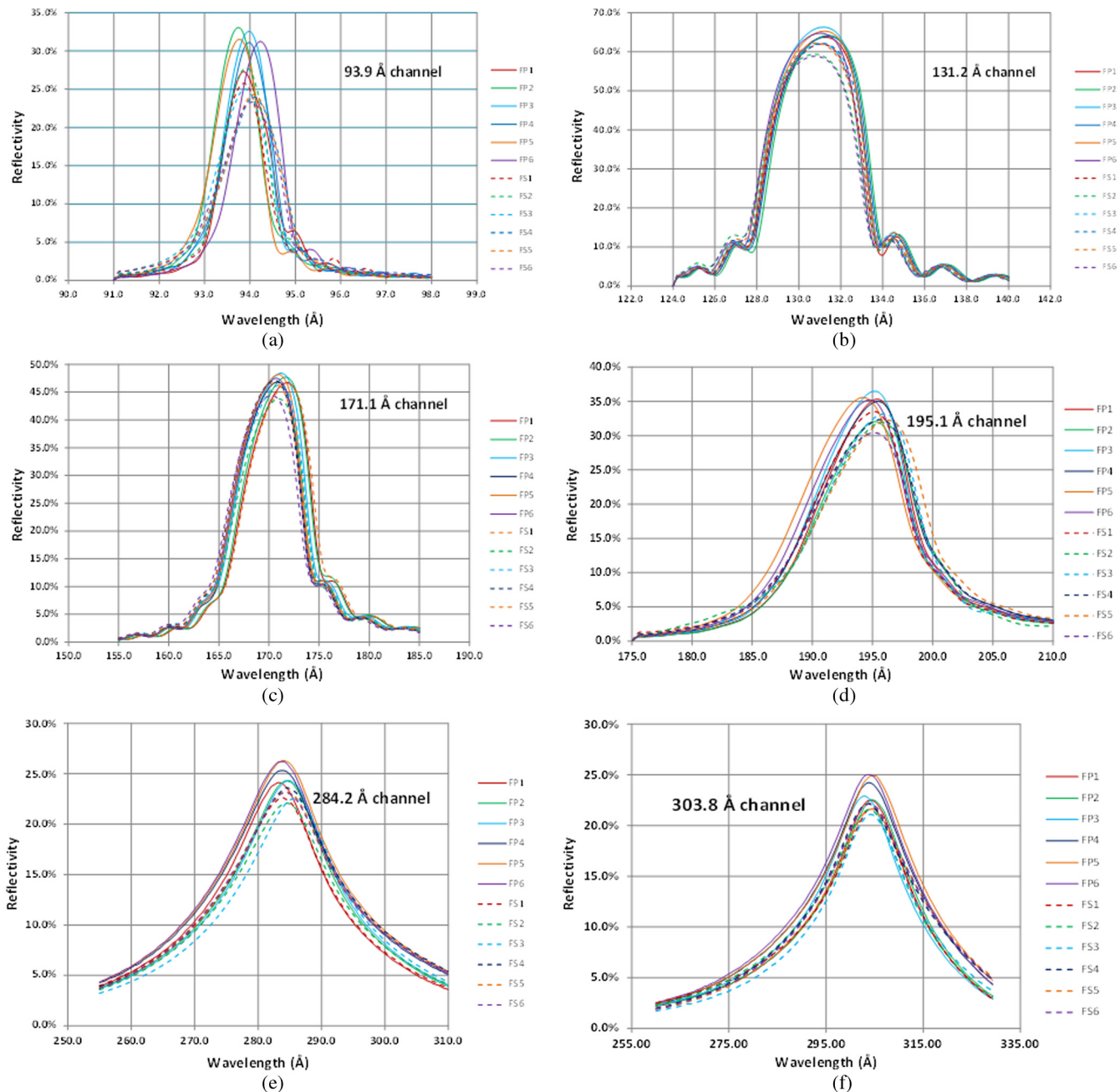


Fig. 12 Area-weighted reflectivity curves for all primary (FP1–FP6, colored solid curves) and all secondary (FS1–FS6, colored dashed curves) flight mirrors measured in each of the six SUVI EUV passbands: (a) 93.9 Å, (b) 131.2 Å, (c) 171.1 Å, (d) 195.1 Å, (e) 284.2 Å, and (f) 303.8 Å.

to the design requirements, the weighted average measured reflectivities exceed predictions in all EUV channels for all SUVI mirrors. SUVI is currently scheduled for launch in 2014.

Acknowledgments

We wish to thank the National Oceanic and Atmospheric Administration's and the National Aeronautic and Space Administration's support for the SUVI program, under NASA contract NNG07HW20C. This work was also, in part, performed under the auspices of the U.S. Department of Energy by Lawrence Livermore National Laboratory under Contract No. DE-AC52-07NA27344, and by the University of California Lawrence Berkeley National

Laboratory under Contract No. DE-AC03-76F00098. The Advanced Light Source is supported by the Director, Office of Science, Office of Basic Energy Sciences, of the U.S. Department of Energy under Contract No. DE-AC02-05CH11231.

References

1. J. Lean et al., "SORCE contributions to new understanding of global change and solar variability," *Sol. Phys.* **230**(1–2), 27–53 (2005).
2. P. Pilewskie, G. Rottman, and E. Richard, "An overview of the disposition of solar radiation in the lower atmosphere: connections to the SORCE mission and climate change," *Sol. Phys.* **230**(1–2), 55–69 (2005).
3. T. N. Woods et al., "Solar extreme ultraviolet irradiance measurements during solar cycle 22," *Sol. Phys.* **177**(1–2), 133–146 (1998).

4. M. Kretzschmar, J. Liliensten, and J. Aboudarham, "Retrieving the solar EUV spectral irradiance from the observation of 6 lines," *Adv. Sp. Res.* **37**(2), 341–346 (2006).
5. U. Feldman and E. Landi, "The temperature structure of solar coronal plasmas," *Phys. Plasmas* **15**, 056501 (2008).
6. J. T. Mariska, *The Solar Transition Region*, Press Syndicate of the University of Cambridge, New York (1992).
7. J. H. Underwood et al., "X-ray photographs of a solar active region with a multilayer telescope at normal incidence," *Science* **238**(4823), 61–67 (1987).
8. A. B. C. Walker, Jr. et al., "Soft X-ray images of the solar corona with a normal-incidence cassegrain multilayer telescope," *Science* **241**(4874), 1781–1787 (1988).
9. L. Golub et al., "Sub-arcsecond observations of the solar X-ray corona," *Nature*, **344**, 842–844 (1990).
10. D. S. Martínez-Galarce et al., "High resolution imaging with multilayer telescopes: resolution performance of the MSSTA II telescopes," *Opt. Eng.* **39**(04), 1063–1079 (2000).
11. J.-P. Delaboudinière et al., "EIT: extreme-ultraviolet imaging telescope for the soho mission," *Sol. Phys.* **162**(1–2), 291–312 (1995).
12. B. N. Handy et al., "The transition region and coronal explorer," *Sol. Phys.* **187**(2), 229–260 (1999).
13. J. R. Lemen et al., "The atmospheric imaging assembly (AIA) on the solar dynamics observatory (SDO)," *Sol. Phys.* **275**(1–2), 17–40 (2011).
14. P. Boerner et al., "Initial calibration of the atmospheric imaging assembly (AIA) on the solar dynamics observatory (SDO)," *Sol. Phys.* **275**(1–2), 41–66 (2012).
15. D. S. Martínez-Galarce et al., "A novel forward-model technique for estimating EUV imaging performance: design and analysis of the SUVI telescope," *Proc. SPIE* **7732**, 773237 (2010).
16. D. S. Martínez-Galarce et al., "Microroughness measurements and EUV calibration of the Solar Ultraviolet Imager multilayer-coated mirrors," *Proc. SPIE* **8501**, 85010I (2012).
17. J. E. Harvey et al., "Image degradation due to scattering effects in two-mirror telescopes," *Opt. Eng.* **49**(6), 063202 (2010).
18. H. Davies, "The reflection of electromagnetic waves from a rough surface," *Proc. IEE - Part IV: Instit. Monog.* **101**(7), 209–214 (1954).
19. J. E. Harvey, K. L. Lewotsky, and A. Kotha, "Effects of surface scatter on the optical performance of x-ray synchrotron beam-line mirrors," *Appl. Opt.* **34**(16), 3024–3032 (1995).
20. J. Harvey et al., "Total integrated scatter from surfaces with arbitrary roughness, correlation widths, and incident angles," *Opt. Eng.* **51**(1), 013402 (2012).
21. D. L. Windt, W. K. Waskiewicz, and J. E. Griffith, "Surface finish requirements for soft x-ray mirrors," *Appl. Opt.* **33**(10), 2025–2031 (1994).
22. M. Trost et al., "Roughness characterization of EUV multilayer coatings and ultra-smooth surfaces by light scattering," *Proc. SPIE* **8501**, 85010F (2012).
23. R. Soufli et al., "Development and testing of EUV multilayer coatings for the atmospheric imaging assembly instrument aboard the solar dynamics observatory," *Proc. SPIE* **5901**, 59010M (2005).
24. R. Soufli et al., "In-band and out-of-band reflectance calibrations of the EUV multilayer mirrors of the atmospheric imaging assembly instrument aboard the Solar Dynamics Observatory," *Proc. SPIE* **8443**, 84433C (2012).
25. R. Soufli et al., "Atomic force microscopy characterization of Zerodur mirror substrates for the extreme ultraviolet telescopes aboard NASA's solar dynamics observatory," *Appl. Opt.* **46**(16), 3156–3163 (2007).
26. R. Soufli et al., "Sub-diffraction-limited multilayer coatings for the 0.3 numerical aperture micro-exposure tool for extreme ultraviolet lithography," *Appl. Opt.* **46**(18), 3736–3746 (2007).
27. D. Windt et al., "Experimental comparison of extreme-ultraviolet multilayers for solar physics," *Appl. Opt.* **43**(9), 1835–1848 (2004).
28. E. M. Gullikson, S. Mrowka, and B. B. Kaufmann, "Recent developments in EUV reflectometry at the advanced light source," *Proc. SPIE* **4343**, 363–373 (2001).
29. M. Snow et al., "EUVS-C: the measurement of the magnesium II index for GOES-R EXIS," *Proc. SPIE* **7438**, 743803 (2009).



Dennis Martínez-Galarce is president and lead consultant of Galapagos Science & Engineering Group where he works on next-generation technologies for remote-sensing. Previously, he worked at the Lockheed Martin Advanced Technology Center (LMATC) as a senior research physicist, leading the optics team on the SUVI program. At the LMATC he also worked on internally-funded programs to develop next-generation EUV/soft x-ray solar instruments that include

large (> 300 mm) SiC EUV optics and microcalorimeters (Transition-edge Sensors). He has been PI on NASA funded programs that

include the use of EUV optics on sounding rockets for solar research and, to study the sun's long-term EUV variation. Prior to the LMATC, he was resident scientist at Stanford University working on the Chandra X-ray Observatory program. He received his PhD and MS degrees in electrical engineering and applied physics from Stanford, and his bachelor degree is in physics and mathematics from Cornell University.



Regina Soufli received her PhD in electrical engineering from the University of California, Berkeley. She was staff scientist at the Harvard-Smithsonian Center for Astrophysics working on NASA's Chandra X-ray Observatory. At Lawrence Livermore National Lab, she has been principal investigator on programs related to extreme ultraviolet (EUV) and x-ray optics for semiconductor lithography, solar physics and astrophysics, synchrotron and free-electron lasers, and high-energy physics. She has recently been developing x-ray optics for the Linac Coherent Light Source (LCLS), the world's first x-ray free electron laser, and EUV multilayer optics for NASA's Solar Dynamics Observatory (SDO) and NASA/NOAA's space weather satellites. Her interests are in EUV/x-ray interactions with matter, surface and materials science, corrosion science, multilayer thin films, roughness and scattering. She is an author of about 100 publications and a book chapter, and has received two "R&D 100" awards.



David L. Windt is the founder and president of Reflective X-ray Optics LLC, and an Adjunct Research Scientist in the Columbia Astrophysics Laboratory at Columbia University. He received his PhD in physics from the University of Colorado in 1987 and has held research positions at Bell Laboratories and the Lockheed Palo Alto Research Laboratory. His research over the past 25 years has focused largely on the development of multilayer X-ray optics for a variety of scientific and technological applications.

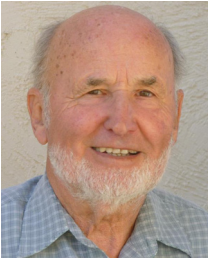
Marilyn Bruner is the CEO of Bermar Science & Technology LLC of Palo Alto, California. Marilyn is a solar physicist with extensive experience in planning and conducting solar research programs from space. She received her BS and MS degrees from the University of Arizona in 1957 and 1959, majoring in physics. She received her PhD in physics from the University of Colorado in 1964. Recently, she concentrated on instrument design with an emphasis on optical design and analysis.



Eric Gullikson received his BS in physics from the University of Hawaii in 1977 and PhD in physics from the University of California, San Diego in 1984. After a postdoc at AT&T Bell Labs, he joined the Center for X-Ray Optics at Lawrence Berkeley National Laboratory in 1987. He has worked on the development of high-accuracy reflectometry and scattering measurement techniques for EUV and soft x-ray radiation. He is author or coauthor of over 200 publications.



Shayna Khatri received her bachelor's degree in optical sciences and engineering from the University of California Davis in 2007. She is currently working with L-3 Communication IOS-Tinsley in project management, with expertise in optical surface metrology and process engineering. Her focus is in metrology and fabrication of precision aspheres for EUV applications as well as manufacturing metal optics for cost-effective telescopes and sub-assemblies.



Eberhard Spiller is the inventor of the multilayer coatings for the EUV and X-ray range and has 40 years of experience in their fabrication and testing. He has used them successfully in astronomical telescopes and EUV cameras. Several EUV solar telescopes now in orbit use multilayer coatings. He also participated in the development of EUV lithography. He spent 25 years at IBM Research in Yorktown Heights and started SPILLER X-RAY OPTICS in 1995.



Jeff C. Robinson has been a member of the technical staff at Lawrence Livermore National Laboratories PLS Optics Group since July 2000. With the laboratory, he has won numerous awards for his work in the field of thin film structures. He has 21 years in electro mechanical experience with vacuum systems and 16 years in thin-film multilayer deposition where he now manages a state-of-the-art laboratory that includes (among many instruments), a DC-magnetron sputtering deposition tool used for precision coatings on large-area optics, the same tool used to coat the SUVI flight optics,

as well grazing-incidence mirrors for free-electron as x-ray lasers, and detector devices. Jeff is an expert on fixture design, fabrication and the custom cleaning processes applied to a variety of optical substrates prior to thin film deposition.

Sherry Baker received an associate degree in electron microscopy from San Joaquin Delta College, Stockton, California. She is an engineering associate at Lawrence Livermore National Laboratory. Her interest is in the application of state-of-the-art metrology techniques to the development of advanced x-ray optical components and systems. Her primary focus has been the characterization of optical components implemented in the development of extreme ultraviolet lithography (EUVL).



Evan Prast received his BS in optical science and engineering as well as his MS in applied science engineering from U.C. Davis. After completing his master's degree, he was employed at L-3 SSG-Tinsley where he was a project engineer responsible for managing the introduction and completion of extremely challenging optical components. Currently at Research Electro-Optics in Boulder, Colorado, he is a product engineer focusing on prototype and new product integration.